Digital Twin Modeling and Simulation of the High-frequency Transformer Based on Electromagnetic-thermal Coupling Analysis

Wang, Zhaoxin; Bak, Claus Leth; Sørensen, Henrik; Silva, Filipe Miguel Faria da; Wang, Qian

Published in:
2022 21st IEEE Intersociety Conference on Thermal and Thermomechanical Phenomena in Electronic Systems (iTherm)

DOI (link to publication from Publisher):
10.1109/iTherm54085.2022.9899628

Publication date:
2022

Document Version
Accepted author manuscript, peer reviewed version

Citation for published version (APA):
Wang, Z., Bak, C. L., Sørensen, H., Silva, F. M. F. D., & Wang, Q. (2022). Digital Twin Modeling and Simulation of the High-frequency Transformer Based on Electromagnetic-thermal Coupling Analysis. In *2022 21st IEEE Intersociety Conference on Thermal and Thermomechanical Phenomena in Electronic Systems (iTherm)* IEEE (Institute of Electrical and Electronics Engineers). https://doi.org/10.1109/iTherm54085.2022.9899628

Multiphysics Digital Model of the High Frequency Transformer for Power Electronics Application Considering Electro-thermal Interactions

Zhaoxin Wang, *Student Member, IEEE*, Claus Leth Bak, *Senior Member, IEEE*, Huai Wang, *Senior Member, IEEE*,
Henrik Sørensen, and Filipe Faria da Silva, *Senior Member, IEEE*,

***Abstract*- The high frequency transformer (HFT) applied in the power electronics operate under the combined stresses of high-frequency PWM voltage and high temperature. The electro-thermal coupling effect can accelerate the aging process and even cause the failure of the HFT's insulation. The accurate modeling and simulation of the multiphysics fields of the HFT is crucial for investigating the electrical and thermal stresses on the insulation. The interaction between the electromagnetic and temperature fields in HFTs makes this task challenging. Specifically, the temperature field in HFTs is influenced by electromagnetic losses, while the electromagnetic parameters of the material and loss distribution are related to temperature and voltage frequency. This paper explores the interaction between high-frequency electromagnetic and temperature fields and develops a comprehensive multiphysics coupling model based on the analyzed results. The model allows for the digital replicate of the circuit, electric, magnetic and temperature fields and it provides precise identification of the electrical and thermal stresses on the insulation. A 60 kHz HFT for dual active bridge (DAB) applications is taken as the example and the simulation results indicate that the proposed model can improve accuracy by 19.14 % compared to conventional methods. Finally, a high-frequency pulse width modulation (PWM) test platform for the HFT is developed, and the proposed model is validated through experimental results.**

Index Term: high frequency transformer (HFT), multiphysics modeling, electro-thermal coupling effect

I. INTRODUCTION

As the voltage level of modern power electronic converters increases, as solid-state transformer (SST) based on medium voltage power switches and DC-DC converters for medium voltage application [1-2], high frequency transformers (HFT) are subjected to higher electrical and thermal stresses. Compared to power frequency transformers, HFTs have the advantages of compact size and high-power density [3]. However, when subjected to pulse width modulation (PWM) voltage for extended periods, HFTs can experience a higher combined stress of electro-thermal [4-5]. This can lead to accelerated aging and failure of the insulation [6], impacting the reliability of the converter. As a result, it becomes necessary to study the multiphysics behavior of the HFT under PWM voltage, to investigate the electro-thermal stresses subject to the insulation, and to identify the weak points of the insulation to accurately predict the remaining lifespan of the HFT and provide a foundation for its optimal design.

Previous research has been conducted on the multiphysics analysis of power frequency transformers [7-9]. In recent year, numerous scientific efforts have also been made to develop physical models for medium to high frequency transformers [10-11].

Dujic conducted a comparative analysis of numerical and analytical models for transformer modeling and proposed a data-driven method for optimal design of medium frequency transformers based on finite element analysis (FEA) [12]. The proposed model employs finite element method (FEM) to simulate the magnetic and electric fields of the transformer, enabling analysis of the impact of geometry on leakage inductance, and identification of maximum electrical stress subject to insulation material. Ultimately, simulation results are trained using regression methods. The simulation and experimental results demonstrate that the proposed model provides a significant improvement in computational speed without compromising accuracy. However, the author does not present the loss model and thermal model in this paper.

Zhao developed separate magnetic and electric model for the high frequency transformer used in a DC-DC converter [13]. The 3D magnetic field is built based on the FEA and examines the impact of different core structures on losses, magnetic field, and leakage inductance carefully. Additionally, a 3D analysis of the electric field is conducted, taking into account air bobbin, encapsulating and insulation tape. The maximum electric field strength subject to the insulation is determined. Based on these findings, a 500 kHz transformer prototype is developed with the required insulation level and optimized magnetic field losses. Experimental results show that the design could achieve high efficiency and power density at the same time compared to other research that focuses only on one factor. The author also does not present the thermal model of the transformer.

Yi [14] introduced a novel method for the insulation design of medium frequency transformers (MFTs). The method focused on optimizing the insulation distance parameters through FEM simulations to enhance the power density while ensuring compliance with insulation requirements. The proposed method was implemented on a 60 kVA/10 kHz transformer, and the simulation results of the electric and temperature fields validated the effectiveness of the proposed approach. A prototype was constructed based on the proposed design, demonstrating the successful operation of the MFT under rated conditions, thereby confirming the viability and efficacy of the proposed insulation design method. But the thermal behavior is not considered in the insulation design of the MFT.

To calculate the fringing losses and to assess their thermal impact on high-frequency planar transformers (PTs), Shafaei [15] modeled the magnetic field and loss of two PTs using FEM. The influence of switching frequency and core width on the fringing losses was studied, and a method was proposed to calculate the fringing losses. The proposed formula was applied to the thermal model to analyze the thermal effect of the fringing effects. Experimental tests were conducted on transformers to evaluate and demonstrate the accuracy of the obtained results, confirming the accuracy of the proposed methodology. However, the authors' use of a lumped parameter model, which is a thermal network characterized by a limited number of discrete parameters cannot capture detailed fluid flow characteristics and does not provide a comprehensive temperature distribution. For a more comprehensive analysis of fluid motion, the approach of computational fluid dynamics (CFD) is required.

Guo [16] conducted a 2D electrostatic simulation on the MFT, wherein the location of the maximum electric field was identified. The partial discharge inception voltage (PDIV) was measured during the partial discharge (PD) test, and the results showed good agreement with the FEM simulation. Furthermore, the author constructed a 3D FEM thermal model to offer a comprehensive and accurate representation of thermal behavior. The temperatures of the core, winding, and potting material surfaces exhibited a strong correlation with the experimental data. Additionally, a sensitivity analysis of the hotspot temperatures was performed, considering variations in the cooling airflow speed based on the developed model. However, the authors neglected to account for the electro-thermal interaction during their modeling of the electrostatic and temperature fields.

Leibl developed thermal and loss models for a 20 kHz water-cooled medium frequency transformer used in a high-power DC-DC converter [17]. A detailed thermal network model was developed to predict the transformer's hot spot temperature and was validated using 3D FEA. The winding loss model was developed with consideration of skin effect and edge effect and validated using 2D finite element analysis. The core loss model was developed using the improved generalized Steinmetz equation (iGSE). The authors suggest that further optimization of the transformer's cooling system using 3D FEA is a promising avenue for future research. Finally, an optimization procedure was proposed to achieve maximum power density and efficiency of the transformer. However, the complex interaction between the electromagnetic and temperature fields was not considered in this paper.

Based on the aforementioned research, it is evident that multiphysics simulation is extensively utilized for thermal management, design optimization, and insulation design of medium and high frequency transformers. However, the existing studies have primarily focused on individual aspects of the transformer, while the bi-directional coupling effects between electrical-thermal behavior in the solid part and thermal-flow in the fluid part are often neglected. Therefore, there is a significant research gap that needs to be addressed to develop an accurate and comprehensive multiphysics model for medium and high frequency transformers.

In this paper, a comprehensive digital model for HFTs is proposed, which integrates the circuit model, magnetic model, electric model, loss model, and thermal-airflow model. Furthermore, the detailed interactions between different models, specifically the effects of temperature and high-frequency pulse-width modulation (PWM) voltage on the electromagnetic loss model and the electromagnetic material parameters of the transformer are investigated. The outcomes of this study have practical implications for the design and performance optimization of HFTs, leading to improved efficiency, reduced losses, and enhanced reliability in various applications.

This paper is organized as follows. Section II introduces the structure of the multiphysics digital framework for HFTs and briefly describes the main principles and functions of each part. Section III describes the multiphysics theory and models of the transformer. Section IV analyze the interaction between electromagnetic and thermal models in detail and provide a bidirectional coupling analysis procedure for the HFT while taking into coupling effect between different models. Taking a 60 kHz HFT as an example, Section V presents simulation results of magnetic field, loss distribution, temperature field, airflow field, and electric field. The electrical and thermal stresses on the insulation and the regions at greatest risk are identified. The accuracy of the simulation is theoretically verified, and a comparison with the conventional method is provided. Section VI introduces the high frequency test platform for the HFT, where the loss and temperature distribution are measured and validated the proposed model. Section VII and VIII provides a discussion and summary of main findings.

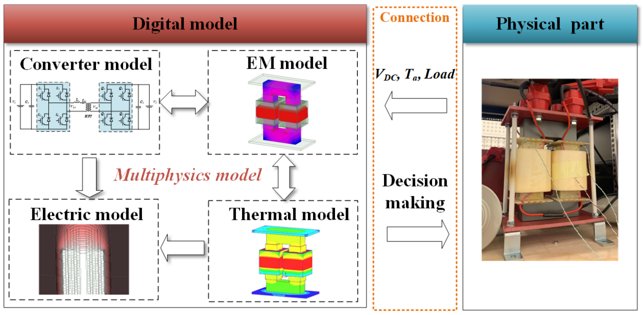

Fig. 1. The framework of the multiphysics digital model.

II. MULTIPHYSICS DIGITAL FRAMEWORK FOR HFTS

The objective of the digital model is to replicate the multiphysics fields of the HFT and aid in identifying the electrical and thermal stresses that applied to the insulation system. The framework of the digital model is shown in Fig. 1. The inputs of the digital model include the DC voltage applied to the primary side of the converter, the ambient temperature, load, control method, and conduction angle of the converter. The output of the digital model could be used for decision-making and improving the performance of the HFT, such as providing a reference for optimal design, predicting remaining lifetime, and assessing reliability of the transformer. For instance, if the simulation results indicate a short remaining life or low reliability of the transformer, appropriate measures can be taken, such as replacing the transformer, adjusting the load, or improving the transformer design.

The model comprises several parts, including electromagnetic, losses, and thermal-airflow field models of the HFT. Each field is coupled with the others to enable coupling analysis, enhancing the accuracy and integration of the digital model. The converter model aims to solve the voltage and current waveforms applied to the HFT in the specific converter circuit diagram based on the circuit theory. The time-varying electromagnetic model aims to solve the electric and magnetic fields of the HFT based on Maxwell equations, and the loss density distribution of the HFT is calculated based on modified Steinmetz's equations according to the magnetic field results. Due to the time scale of the electromagnetic problem (microseconds) being much smaller than that of the thermal problem (minutes), the time-average losses are used as the heat source to solve the steady-state thermal problem of the HFT. The steady-state thermal-airflow model aims to solve the temperature and airflow fields of the HFT based on Navier–Stokes equations and heat transfer equations.

III. MULTIPHYSICS MODELLING OF HFTS

To digitally replicate the electric, magnetic, loss, temperature and airflow fields of the transformer, the finite volume method (FVM) is applied to develop its multiphysics field model.

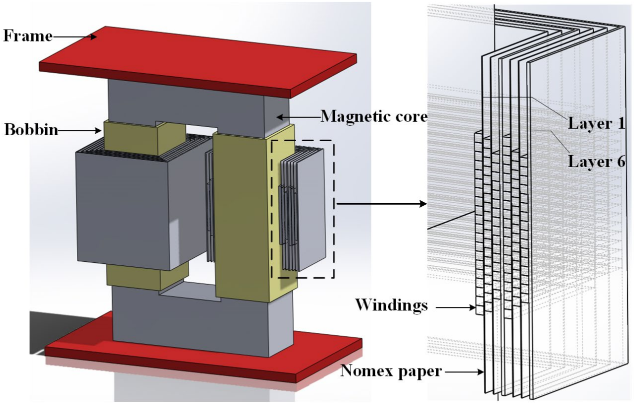

Fig. 2. The 3D geometry of the HFT.

TABLE I
THE MATERIALS USED IN THE HFT

Part	Material
Magnetic core	Ferrite LP3
Windings	Litz wire
Insulation between layers	Nomex paper
Tube	Silicone
Bobbin	Durethan

TABLE II
THE MATERIAL PROPERTIES

Parameters	Copper	Ferrite	Nomex paper	Air
Mass density (kg/m^3)	8933	4800	880	1.1614
Relative permittivity	1	12	3.873	1.0006
Relative permeability	0.99	B-H curve	1	1
Bulk conductivity (S/m)	$\frac{5.96\times10^7}{1+0.00393(T-20)}$	0.01	1.67×10^{-15}	0
Thermal conductivity (W/m·C)	400	4	0.24	0.0261
Specific heat (J/kg·C)	385	750	1349.96	1005
Thermal expansion coefficient (1/C)	1.77×10^{-5}	1×10^{-5}	1×10^{-5}	0.00333
Dynamic viscosity (kg/m·s)	-	-	-	1.84×10^{-5}

Electro-thermal bi-directional coupling and field-circuit coupling methods are applied to improve the accuracy of the model.

In this paper, the proposed model is demonstrated using a 60 kHz dry-type HFT that is used in a dual active bridge (DAB) converter as an example. A 3D geometric model of the HFT containing the magnetic core, windings, insulation, base, and bobbin is built, as shown in Fig. 2. Both primary and secondary windings are arranged in six layers, with 20, 19, 16, 20, 19, and 16 turns respectively for each layer. Litz wire is used for the windings. A litz wire bundle contains 120 of strands, it is difficult to model strands with FVM. Therefore, the windings are modeled as a single object, which is achieved by defining the conductors as litz wire with the strands size and number of strands are specified. The Nomex paper is used as the insulation between winding layers, with each layer having a thickness of 0.12, 0.12, 0.36, 0.12, 0.12, and 0.36 mm, respectively. The ferrite LP3 is used as the material of the magnetic core. The materials used in the HFT are given in Table I. The properties of the main material used for the HFT is given in Table II.

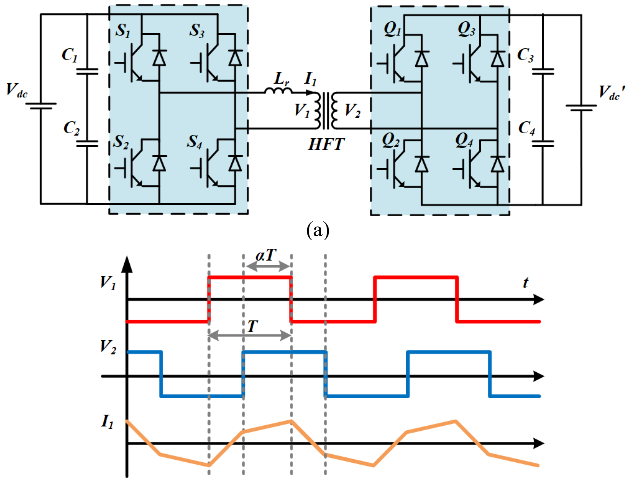

Fig. 3. A DAB converter containing a HFT. (a) The topology of the converter. (b) The principle of the converter.

A. Converter Model

As the excitations for the multiphysics analysis, the voltage and current applied to the high frequency transformer are determined by the topology, loads, and control methods of the converter. The current flowing through the winding also varies with the temperature which will therefore affect the multiphysics analysis. Therefore, the converter model coupled with multiphysics is built to accurately implement the digital model of the HFT under different operating conditions.

The topology and principle of a DAB converter containing a HFT is present in Fig. 3. The AC sides of the two H-bridge converters are connected via the HFT. The H-bridge converter generates a high-frequency square wave voltage on the AC side. The magnitude and direction of power flow can be adjusted by changing the phase shift between the two AC sources. V_{dc} and V_{dc}' are the DC side voltages of the H-bridge on both sides of the converter, respectively. V_1 and V_2 are the AC side voltages of the H-bridge on both sides, respectively. I_{h1} is the primary side current of the HFT. T is half of the switching time of a circle; α is the ratio of the phase shift times between V_1 and V_2.

The ANSYS Simplorer is applied to solve the converter model. Simplorer is a multiphysics circuit simulator that integrates electrical components and allows for coupling FEM electromagnetic models. The minimum and maximum time step of the simulation is set to 10^{-6} s and 10^{-5} s, respectively. The simulation time is set to 1 s. The CPU used in the simulation is Intel Core i7-10610U processor with a clock speed of 1.80GHz, 2304 MHz, 4 Cores, 8 Logical Processors. The CPU time for one iteration is 7.58 seconds. CPU time is a measure of computational resources consumed by the simulation. Within ANSYS, CPU time for one iteration is obtained through the software's built-in monitoring and reporting capabilities. ANSYS records the CPU time for each iteration during the simulation and provides the information in the log files.

B. Electromagnetic Model

The time-varying electromagnetic field is governed by Maxwell's equations, which could express as vector form

$$\nabla \cdot \boldsymbol{E} = \frac{\rho}{\varepsilon_0} \tag{1}$$

$$\nabla \cdot \boldsymbol{B} = 0 \tag{2}$$

$$\nabla \times \boldsymbol{E} = -\frac{\partial \boldsymbol{B}}{\partial t} \tag{3}$$

$$\nabla \times \boldsymbol{B} = \mu_0 \boldsymbol{J} + \mu_0 \varepsilon_0 \frac{\partial \boldsymbol{E}}{\partial t} \tag{4}$$

where E is the electric field strength vector, B is the magnetic flux density vector, J is the current density vector, ρ is the charge density, ε_0 is the permittivity of vacuum, and μ_0 is the permeability of vacuum. Some parameters are frequency and temperature dependent. The interaction between electromagnetic and thermal fields will be discussed in Section IV.

To solve the electromagnetic field with FVM, the magnetic vector potential A and the electrical voltage V are introduced, which are defined by

$$\boldsymbol{B} = \nabla \times \boldsymbol{A} \tag{5}$$

$$\boldsymbol{E} = -\nabla V \tag{6}$$

The transient magnetic field equations of the HFT are derived as

$$\nabla\left(\frac{1}{\mu}\nabla A\right) - \sigma(T)\frac{\partial A}{\partial t} = -\sigma(T)V_s \tag{7}$$

$$A\Big|_{\Gamma_D} = A_0 \tag{8}$$

where μ is permeability, σ is electrical conductivity, V_s is the voltage excitation that varies with time. The material characteristics having a significant thermal dependency are indicated by the presence of the temperature variable T.

$A|_{\Gamma D}=A_0$ is the Dirichlet boundary condition, which means the magnetic field lines are parallel to these boundaries. The unconstrained boundaries are Neumann boundaries, which means the magnetic field lines are perpendicular to these boundaries.

$$\nabla\left(\varepsilon\frac{\partial}{\partial t} + \sigma\right)\nabla V = 0 \tag{9}$$

$$V\Big|_{\Gamma_D} = u(t) \tag{10}$$

Where ε is the permittivity, $V|_{\Gamma D}=u(t)$ is the Dirichlet boundary condition. The Neumann boundary condition is applied to free boundary surfaces, which means the electric field vectors are perpendicular to this boundary. The excitations of the electromagnetic field are voltage and current waveforms calculated from the converter model.

The electromagnetic field is solved with Maxwell transient magnetic and transient electric modules [18]. Maxwell is an electromagnetic field solver for electric machines, transformers and other electric mechanical devices. Considering both the accuracy and time cost of the simulation model, the tetrahedral meshing method is applied to divide the computational domain. The maximum length of the grid is set to 4.5, 0.6, 0.6, and 35 mm for the magnetic core, windings, Nomex paper, and air region, respectively. The mesh refinement studies are conducted to ensure that the grid is fine enough to provide accurate results.

The maximum time step is set to 1 μs, which is less than one-tenth of each waveform period to ensure the accuracy of the simulation. The simulation time is set to 83.35 us, allowing for the analysis of five voltage cycles to capture the changing loss waveform over time. Since the electromagnetic field model is time-varying and the thermal model is steady-state, it is necessary to average the loss waveforms for one voltage cycle to use as the heat source in the thermal model. The time-varying solver is employed for the electromagnetic analysis because a steady-state solver cannot handle the time-varying magnetic field and accurately calculate losses considering the impact of high frequency. The CPU time for one iteration of the electric and magnetic fields is 12.47 and 13.12 hours, respectively.

The simulation time is related to several factors including model complexity, physics and analysis type, solver settings, and simulation time span. The complexity of the simulation model, including the number of elements, nodes, or cells, can significantly impact simulation time. In the case of the HFT model considered in this study, the inclusion of fine insulation paper geometry necessitates a detailed mesh for obtaining accurate results, leading to longer simulation times. Different physics and analysis types have varying computational requirements. Solving circuit models, electromagnetic field models and thermal models have different computational needs. Simulating time-varying fields generally takes more time compared to steady-state fields. The settings configured for the solver in ANSYS can affect simulation time. Typically, a time step is selected to be less than one-tenth of a cycle to ensure solution accuracy. Simulating longer time periods may require more computational time. Considering the specific requirements and needs of the customer, it is vital to achieve a delicate balance between accuracy and simulation time.

C. Thermal Model

The heat transfer in the HFT includes convection, conduction, and thermal radiation. For dry-type transformers, convection plays an important role in heat transfer among them. Solving the heat convection from all surfaces of the HFT is the key to calculating the temperature distribution inside the HFT. However, the convection heat transfer is dependent on the local fluid temperature next to the surface of the HFT, which again is dependent on surface temperature and local flow field. To consider the thermal interaction between the solid and fluid, the conjugate heat transfer is applied to solve the thermal problem of the HFT. The airflow field is governed by the Navier-Stokes equations (mass conservation, momentum conservation, and energy conservation) [19]

$$\nabla \cdot (\rho V) = 0 \tag{11}$$

$$(V \cdot \nabla)V - \nu\nabla^2 V = -\frac{1}{\rho}\nabla p + g \tag{12}$$

$$\nabla \cdot \left(\rho c_p V T\right) - \nabla \cdot (k \cdot \Delta T) = q \tag{13}$$

where t is time, V is the velocity vector of the air, ν is the kinematic viscosity, p is pressure, ρ is the density of air, g is the acceleration of gravity, C_p is the specific heat capacity, T is the temperature, k is thermal conductivity, q is heat source density. The heat conduction in the solid components is as follows [20]

$$-\nabla \cdot (k \cdot \Delta T) = Q \tag{14}$$

where Q is the heat energy flux.

The viscous model is set to laminar flow as the Grashof number (Gr) is calculated 3.38×10^7, which is lower than 10^9. In addition to convection, thermal radiation also exists between bodies. The discrete ordinates model is applied to solve the thermal radiation of the HFT.

The boundary conditions are set to opening boundaries placed at boundaries of the air region to allow air to flow in or flow out depending on the pressure field. The interface boundary condition is set at the solid-fluid interface, which specifies the continuity of the temperature and heat flux of the solid and airflow in the vicinity of the interface. The zero velocity vector field were imposed for initial domain conditions and the boundaries. The pressure is specified as the standard atmospheric pressure of 101325 Pa. The heat source of the thermal-airflow model is the time-averaged loss density distribution of the HFT calculated from the electromagnetic model.

The Icepak steady state thermal and flow module of ANSYS electronics software based on FVM is applied to solve the

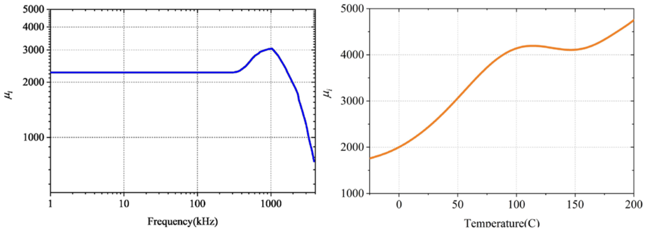

(a) (b)

Fig. 4. The initial permeability characteristics. (a) The initial permeability-frequency (μ_i–f) characteristics. (b) The initial permeability-temperature (μ_i–T) characteristics.

thermal-airflow model [21]. Ansys Icepak is a Computational Fluid Dynamics (CFD) solver that specializes in predicting airflow, temperature, and heat transfer in electrical equipment. The CPU time for one iteration is 7.25 min.

IV. Electro-Thermal Interactions Analysis

The interaction between the electromagnetic and thermal fields results from two aspects, namely the influence of temperature and voltage frequency on the material parameters and losses. In this section, the effects of thermal and voltage frequency on the multiphysics will be analyzed. After that, the bidirectional coupling method is proposed based on the analysis results.

A. The Influence on Material Properties

1) Electrical Conductivity

The electrical conductivity of copper is significantly influenced by temperature. The reciprocal of conductivity, the electrical resistivity p could be expressed as [22]

$$\rho = \rho_{ref}\left(1+\alpha_{ref}\Delta T+\beta_{ref}\Delta T^{2}+\gamma_{ref}\Delta T^{3}\right) \tag{15}$$

$$\Delta T = T - T_{ref} \tag{16}$$

where ΔT is a temperature difference, T is reference temperature, for copper, ρ_{ref}=1.7·10^{-8} Ω m, α_{ref}=2.3·10^{-2} K^{-1}, β_{ref}=2.2·10^{-6} K^{-2}, γ_{ref}=-2.2·10^{-6} K^{-3}.

the equation could be reduced to a first order hyperbolic function

$$\sigma = \frac{1}{\rho} = \frac{\sigma_{ref}}{1+\alpha_{ref}\Delta T} \tag{17}$$

where σ_{ref}=5.8·10^{7} S m^{-1}, α_{ref}=3.9·10^{-3} K^{-1}.

2) Magnetic permeability

The magnetic permeability of the magnetic material is temperature and voltage frequency dependent. The magnetization curve (B-H) of the core is nearly linear in the range of 0-0.4 T at different temperatures. The preliminary simulation results indicate that the maximum B is much less than 0.4 T. Therefore, initial permeability, which is the relative permeability of a material at low values of magnetic flux density, could use in the electromagnetic analysis. The initial permeability-frequency (μ_i–f) and initial permeability-temperature (μ_i–T) characteristics are given in Fig. 4. It shows that the permeability remains constant over a large range under 300 kHz. The operating frequency of the HFT used in this model is 60 kHz. Therefore, the initial permeability is assumed to be constant in the rated operation ranges while the nonlinear characteristics of the magnetic material are considered with the temperature.

B. The Influence on HFT Losses

1) Winding Loss

The loss density in the windings is present as

$$q = \frac{J^{2}}{\sigma} \tag{18}$$

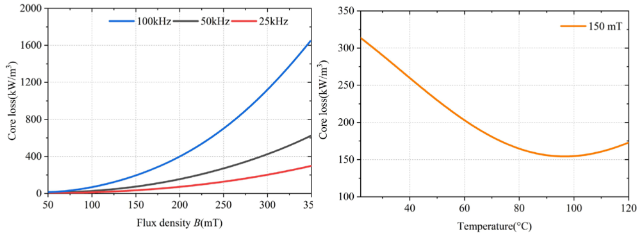

(a) (b)

Fig. 5. The core loss characteristics (a) at different frequencies when the temperature is 60 °C and (b) at different temperatures when B is 150 mT.

with FVM method, the loss density in a volume Ω_e could be given as

$$q = \frac{1}{\Omega_e}\int_{\Omega_e}\frac{J^{2}}{\sigma}d\Omega \tag{19}$$

when the current density in the windings is described by voltage, Equation (19) becomes

$$q = \frac{1}{\Omega_e}\int_{\Omega_e}\sigma\left(V_s+\frac{\partial A}{\partial t}\right)^{2}d\Omega \tag{20}$$

The skin effect and proximity effect will influence the current density in the conductor and result in additional losses. Both skin losses and proximity losses increase with the increase of the frequency. Therefore, the windings loss is temperature and frequency dependent.

2) Core Loss

Steinmetz equation is widely used to evaluate the core loss when the magnetic core is magnetized with a sinusoidal wave excitation, as shown as [23]

$$P_c = k\cdot f^{\alpha}\cdot {B_m}^{\beta} \tag{21}$$

where k, α, and β are the Steinmetz parameters that could obtained from the B-P curves provided by the manufacturer.

However, the HFT employed in power electronics often suffers from non-sinusoidal excitations. For the square voltage or the trapezoidal wave excitations, the modified Steinmetz equation with the waveform coefficient FWC is used to correct the Equation (21), as present in [24]

$$P_c = FWC\cdot k\cdot f^{\alpha}\cdot {B_m}^{\beta} \tag{22}$$

when the excitation is square wave

$$FWC = \frac{\pi}{4}\cdot(2-D) \tag{23}$$

where D is duty cycle

The Steinmetz parameters used for the simulation are calculated from the core loss characteristics (B-P curves), which are determined by both frequency and temperature. The core loss characteristics with the frequency and temperature are shown in Fig. 5.

Based on the above analysis, it is clear that material parameters and loss models for electromagnetic field calculations are affected by temperature and frequency. Neglecting their effects in the calculations may result in large errors, and their relationships are nonlinear, making it difficult to describe them using analytical models. Therefore, a magnetic-thermal bi-directional coupling method is proposed. The flowchart is present in Fig. 6. The process of the method is as follows.

1. Build the time-varying electromagnetic model of the HFT. Set the initial temperature for the 1st iteration. Define the electromagnetic characteristics of the material and the loss calculation model of the HFT. The parameters are updated according to the analysis in Section 4.2. Set boundary conditions, simulation time, and time step.

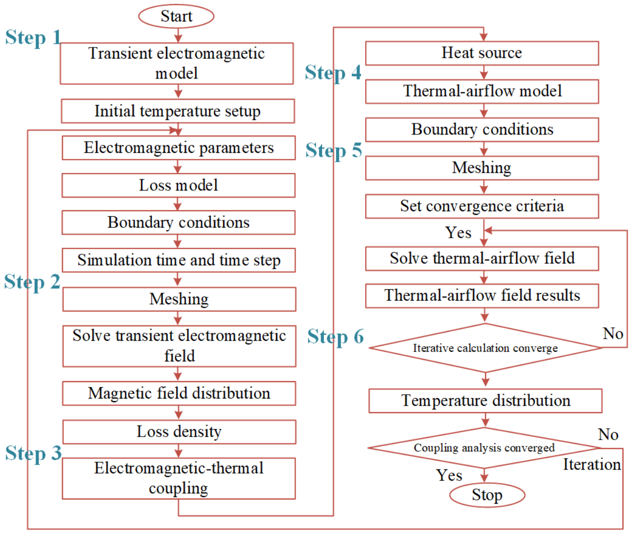

Fig. 6. The flowchart of the electromagnetic-thermal two-way coupling analysis.

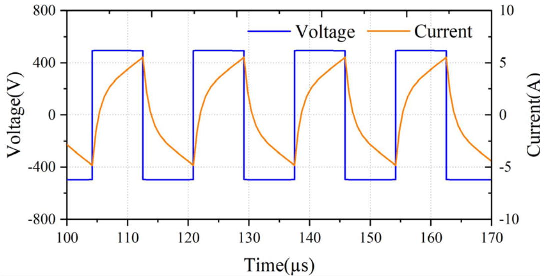

Fig. 7. Voltage and current waveforms applied to the HFT.

2. Define the element length for each part of the HFT and divide the mesh. Solve the electromagnetic field of the HFT. Conduct mesh refinement study to check if the mesh is sufficient, if not, refine the mesh and recalculate. Mesh refinement study is only performed on the first iteration.
3. Couple the time-average loss density distribution to the thermal-airflow field model as the heat source.
4. Build the steady state thermal-airflow model of the HFT. Set the boundary conditions.
5. Divide the mesh and set the convergence criteria for the thermal model. For this model, flow, energy, and discrete ordinates residuals are set to 10^{-3}, 10^{-7}, and 10^{-6} respectively. Iteratively solve the thermal-airflow model until the convergence criteria are satisfied. Conduct mesh refinement study in the 1st iteration.
6. Couple the temperature distribution of the HFT to the electromagnetic model. Update the material characteristics and the loss model. Solve the magnetic field with the updated parameters until the relative error between two adjacent iterations is less than 0.1 %. The total loss of the HFT is used to determine if the coupling analysis is converged, as shown in Equation (24).

$$\frac{\left|L_{n+1}-L_{n}\right|}{L_{n}}<\delta \tag{24}$$

where n is the number of iterations, and the minimum iteration is two.

V. SIMULATION RESULTS

A. Converter Model

For this model, the phase shift control method is applied for the DAB converter. The switching frequency of the H-bridge circuits on both sides is 60 kHz. The conduction angle is set to 180° to generate a square wave voltage with a duty cycle of 50 %.

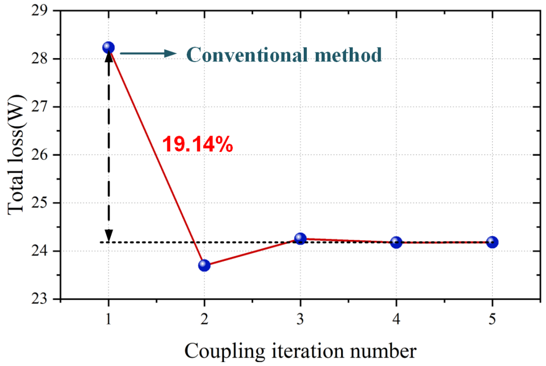

Fig. 8. The total loss for each iteration.

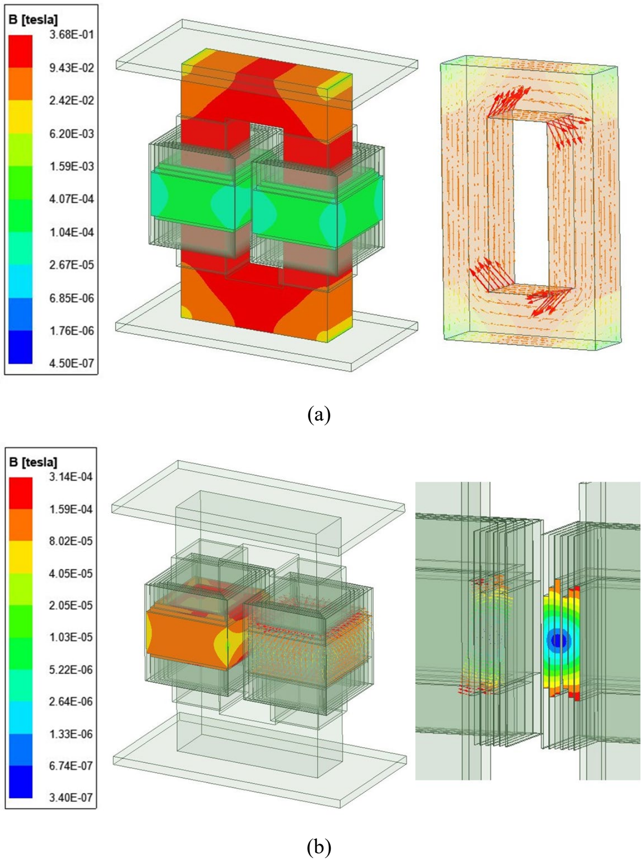

(a)

(b)

Fig. 9. *B* field distribution (a) in the core. (b) in the windings.

TABLE III
COUPLING SIMULATION RESULTS OF THE MAGNETIC FIELD

Coupling iteration	Winding loss (W)	Core loss (W)	Total loss (W)	Relative error (%)
1	26.766	1.471	28.229	-
2	22.302	1.396	23.695	19.14
3	22.824	1.423	24.251	2.29
4	22.752	1.419	24.174	0.32
5	22.752	1.420	24.179	0.02

The voltage and current waves on primary side of the HFT when V_{DC} is 500 V are shown in Fig. 7. The results are coupled to the electromagnetic model as the excitation to solve the multiphysics of the HFT.

B. Magnetic Model

After 5 iterations, the relative difference of the total losses between two adjacent coupling simulations is less than 0.1 %, which indicates the convergence of the coupling analysis. The simulation results for 5 iterations are given in Table III. The total

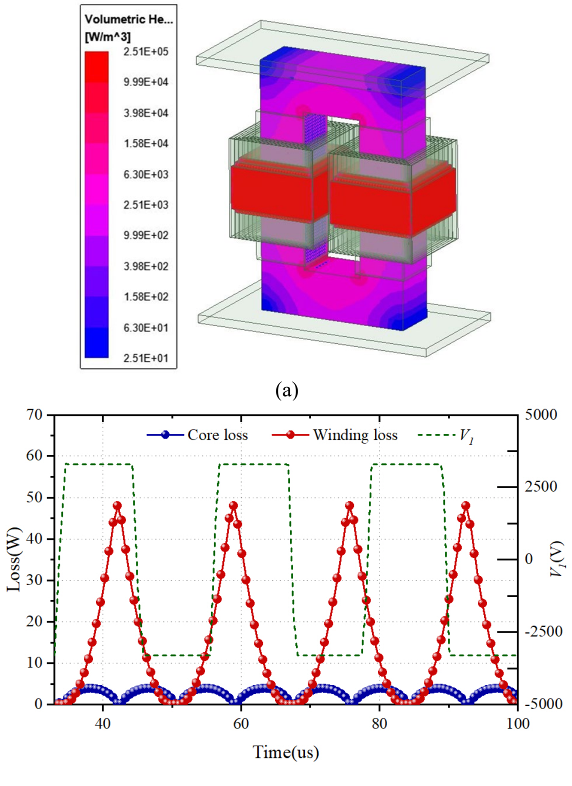

(a)

(b)

Fig. 10. The electromagnetic loss results. (a) the HFT loss waveforms. (b) the loss density distribution.

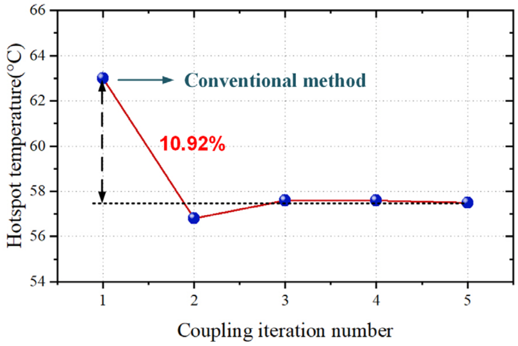

Fig. 11. The hotspot temperature for each coupling iteration.

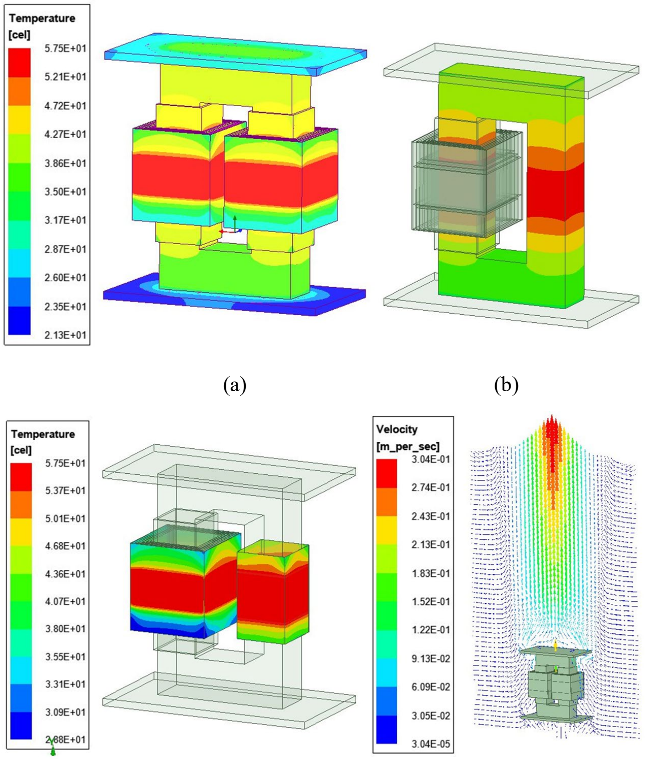

(a) (b)

(c) (d)

Fig. 12. The thermal-airflow field results for the 5th iteration. (a) the temperature distribution of the overall transformer. (b) the temperature distribution of the magnetic core. (c) the temperature distribution of the insulation. (d) the air flow velocity vector distribution in the air.

TABLE IV
THE THERMAL-AIRFLOW FIELD RESULTS FOR EACH ITERATION

Coupling iteration	Maximum temperature in the core (°C)	Maximum temperature in the windings (°C)	Maximum velocity of the air (m/s)
1	66.6	63.0	0.321
2	82.0	56.8	0.302
3	86.3	57.6	0.303
4	87.7	57.6	0.304
5	88.1	57.5	0.304

loss with the number of coupling iterations is shown in Fig. 8. The proposed magnetic-thermal bi-directional coupling method improves the accuracy by 19.14 % compared to the conventional one-way coupling method, which neglects the interaction between electromagnetic and temperature fields.

According to the analysis in Section III, as the temperature rises, the conductivity of the copper decreases and the voltage on the primary side of the HFT remains constant, so the winding copper loss also decreases. Fig. 4b indicates that an increase in temperature leads to an increase in flux density B of the core, which will in turn results in an increase in core loss. However, as demonstrated in Fig. 5b, the core loss per unit volume increases with rising temperature for a particular level of flux density. In summary, the total core loss is related to both flux density and loss per unit volume, which leads to a non-linear relationship between total core loss and temperature. The loss model has a greater impact than the role of magnetic permeability, causing the loss to appear to decrease. As the result, the loss results display a trend of initially decreasing and then fluctuating to level out.

The results of the 1st coupling calculation (using the conventional one-way coupling method) have high losses and significant errors due to its use of a constant ambient temperature in determining the parameters. After two coupling iterations, the temperature field distribution of the transformer was used to correct the material parameters and the loss model, leading to a significant improvement in the calculation results.

The magnetic field results for the 5th iteration when B reaches the maximum value in a voltage period are shown in Fig. 9. The maximum B of the core reaches 0.368 T, which occurs at the inner corners of the core legs. The maximum leakage B in the windings is 3.14×10^{-4} T. It is noticed that leakage flux density at the outer sides of both primary and secondary windings is higher, which is commonly known as edge-effect. That means the magnetic field at the edge of the winding produces a concentration of current density at the edges of the windings, and this effect could cause additional high local eddy current losses in the windings [25]. The electromagnetic loss curve with the time and time-average loss density distribution of the HFT are presented in Fig. 10.

C. Thermal Model

The simulation results of the thermal-airflow field for each iteration are given in Table IV. The hotspot temperature curves

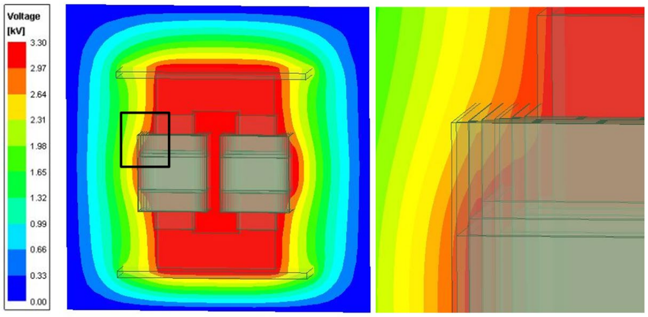

Fig. 13. The voltage distribution.

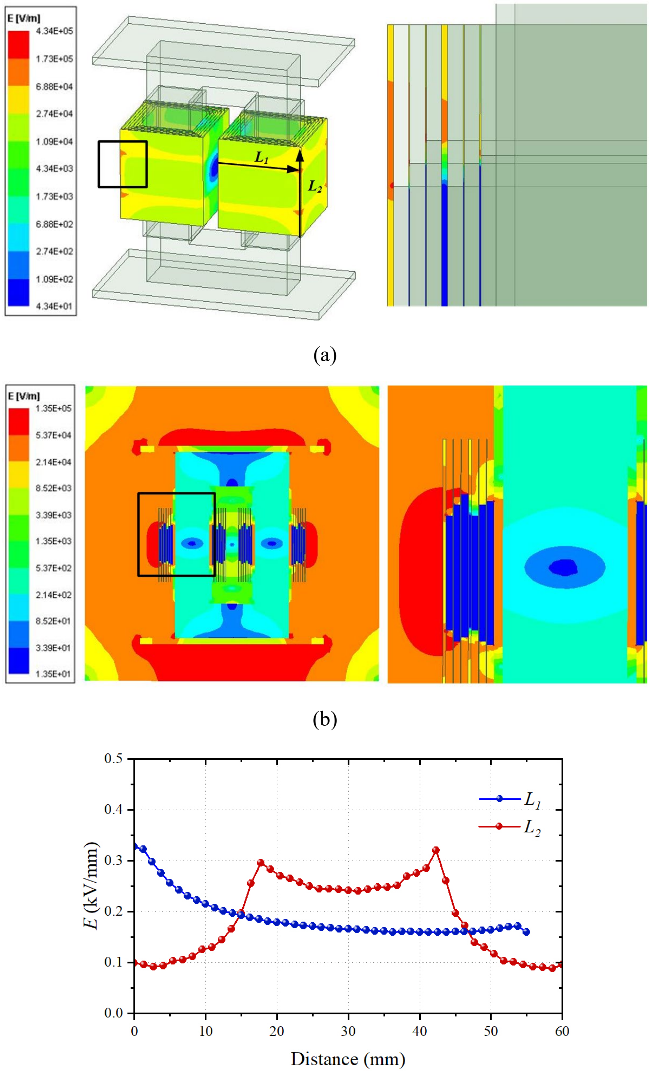

(a)

(b)

(c)

Fig. 14. The electric field distribution (a) of the insulation. (b) on the x-y plane. (c) along line L_1 and line L_2. (Line L_1 and L_2 are shown in figure a).

for each iteration are present in Fig. 11. The hot spot temperature calculated from the proposed model can significantly improve the accuracy by 10.92% compared to the conventional method. The temperature and airflow fields result for the 5th iteration are shown in Fig. 12. The hotspot of the HFT is located on the windings with the temperature is 57.5 °C. The air flows in from the bottom and around the transformer and flows out from the top. The middle part of the insulation connected to the winding is subjected to large thermal stresses due to its proximity to the heat source and poor heat dissipation conditions. In addition, the upper end of the insulation has a higher temperature compared to the lower end.

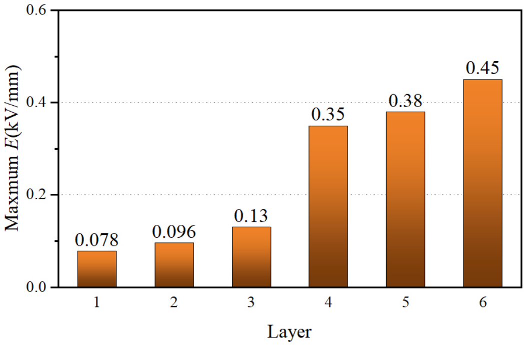

Fig. 15. The maximum E on the surface of each insulation layer.

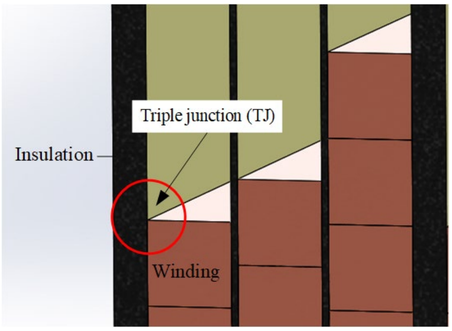

Fig. 16. The triple junction of winding, insulation, and air.

D. Electric Model

The voltage distribution in the X-Y plane when V reaches its peak value in one voltage cycle is shown in Fig. 13. The number of turns in each winding layer varies, resulting in different longitudinal lengths for each winding layer. The displacement of the winding ends leads to a large potential gradient in the vicinity, resulting in the insulation layer near the winding ends being subject to a large electric field strength. The electric field distributions when maximum E reaches its peak value in a voltage period is present in Fig. 14. The maximum E on the insulation surface occurs at the 6th insulation layer, adjacent to the end of the winding layer. The maximum electrical stress subjected to each layer of the insulation is given in Fig. 15.

Based on the simulation results, it is evident that the triple junction of winding, insulation, and air suffers a strong electric field, making it the most critical region for partial discharge (PD) and accelerated aging. PD is a local discharge phenomenon, occurring when a small portion of the insulation material experiences a temporary breakdown [26]. This phenomenon can potentially accelerate the aging process and ultimately result in the failure of the insulation system. This "triple junction" is a critical area from a dielectric perspective as mentioned in [27], as shown in Fig. 16. The difference in permittivity between air and insulation paper results in an amplification of the electric field in the air. Additionally, the amplification of the electric field vector is significantly impacted by dielectric refraction when intersections between dielectrics with different permittivity occur at non-perpendicular angles. In such scenarios, if the local electric field conditions exceed a critical threshold, it may lead to the occurrence of surface discharge [28]. PDs can cause the insulation to age faster, and the charges that accumulate on the insulation's surface can alter the spatial distribution of the electric field [29]. Ultimately, the presence of PDs may shorten the lifetime of the transformer.

The core of the power frequency transformer is required to be grounded at one point to avoid floating potentials and the consequent discharge [30-31]. In applications where stringent isolation is paramount, such as in HFTs, grounding the core can introduce additional capacitance between the windings,

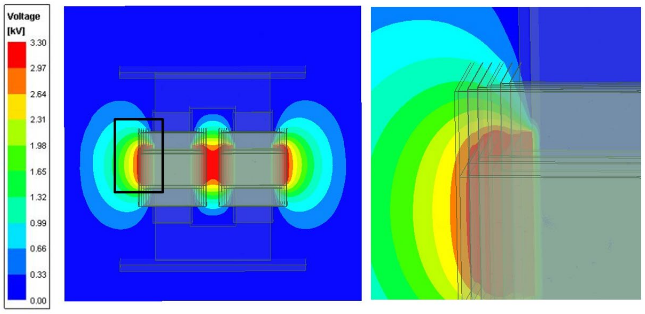

Fig. 17. The voltage distribution.

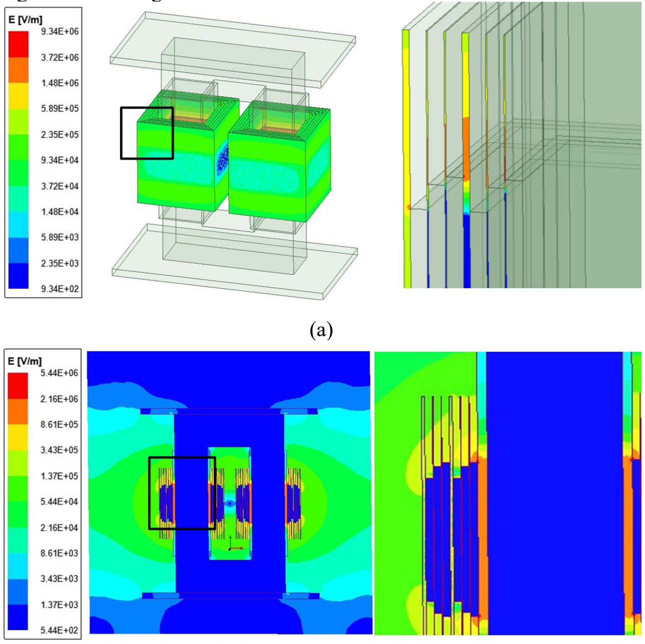

(a)

(b)

Fig. 18. The electric field distribution when the magnetic core is grounded (a) of the insulation. (b) on the x-y plane.

impacting impedance characteristics and promoting coupling between them. This effect becomes more significant at higher frequencies. The HFT utilized in this study uses ferrite as the core material, which has a high resistivity. However, for metal soft magnetic material, such as nanocrystalline with low resistivity, they should be taken as conductor and connected to the ground [32]. Consequently, the decision to ground the core for the HFT should be based on a comprehensive analysis of the specific requirements and design considerations of the transformer and converter system in use.

Therefore, this study also includes simulations of the core grounded to investigate the impact on the electric field of the HFT, as well as the resulting electrical stress imposed on the insulation. The voltage and electric fields result when the magnetic core is grounded are shown in Fig. 17 and Fig. 18, respectively. The other parameters, such as dimensions, materials, and excitations of the HFT and simulation setup remain the same. It is evident from the figure that the electric field distribution has changed significantly when the core is grounded. Grounding the core leads to a reduction in the electric field strength withstood by the frame, while the electric field strength around the bobbin increases. It is noteworthy that the location where the insulation experiences the highest electrical stress changes from the 6th layer, located farther from the core to the 1st layer in proximity to the core, and the distribution of the electric field becomes more concentrated. The maximum electric field strength still occurs at the winding end for each layer of insulation. Therefore, in the case of grounding considerations for this type of HFT, it is advisable to increase the thickness of the 1st layer of insulation to prevent discharge and accelerated aging resulting from excessive local electric field strength.

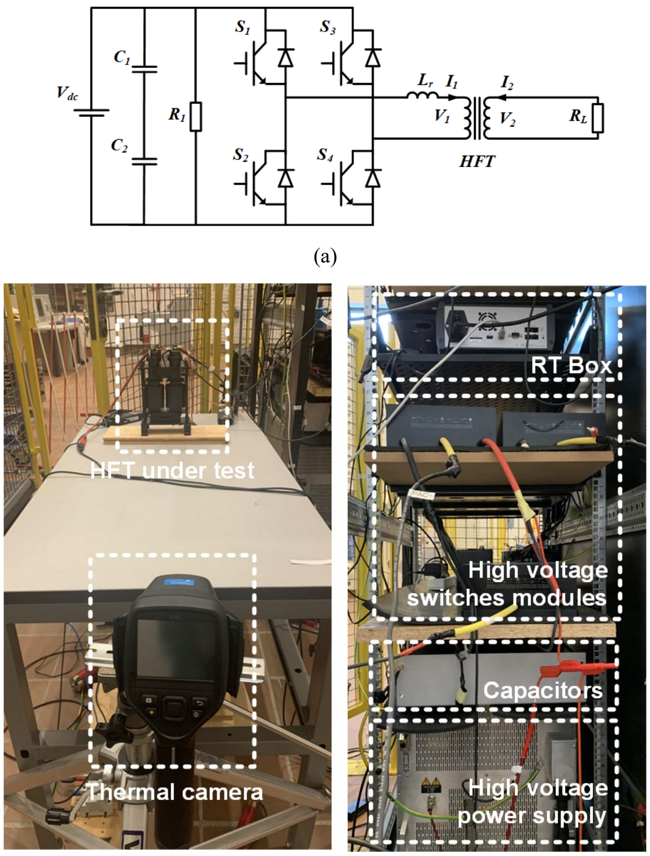

(a)

(b)

Fig. 19. HFT test platform. (a) the circuit diagram of the platform. (b) the hardware realization of the platform.

E. Theoretical Verification

Mesh refinement study is conducted to evaluate the discretization error and to check if the developed mesh is sufficiently refined.

The mesh refinement study is carried out based on a comparison of the simulation results for three meshes (coarse, medium, and fine). Based on the results obtained for three meshes, the grid convergence index (GCI) method can determine the order of convergence to estimate the asymptotic solution and the bounds for discretization error objectively [33].

The GCI is defined as

$$GCI = \frac{F_s|\varepsilon|}{r^p - 1}100\% \tag{25}$$

where F_s is a safety factor, which is 1.25 for three meshes. ε is the quantity that defines the relative difference between sequent solutions, as described in

$$\varepsilon = \frac{f_1 - f_2}{f_1} \tag{26}$$

where f is the quantity that represents the calculation result that characterizes the response of the system. r is the effective grid refinement ratio, and is defined as

$$r = \left(\frac{N_1}{N_2}\right)^{\frac{1}{D}} \tag{27}$$

where N_i is the total number of grid points used for the i-th grid; D is the dimension of the domain. P is the order of convergence, and is given by

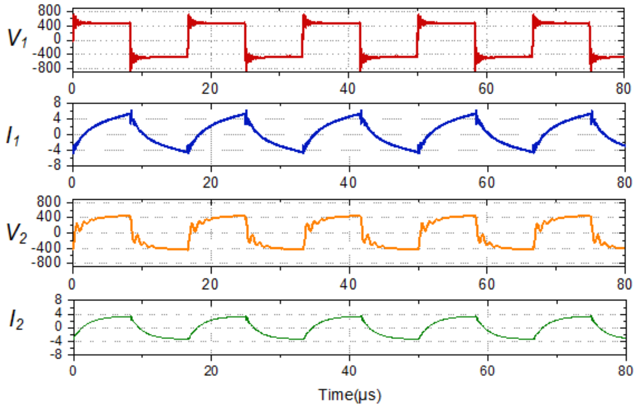

Fig. 20. Voltage and current waveforms on both sides of the HFT.

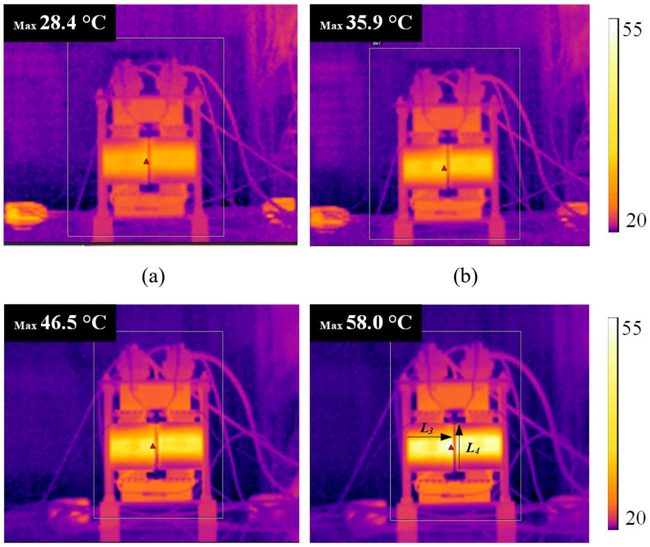

(a) (b)

(c) (d)

Fig. 21. Surface temperature distribution of the HFT when (a) V_{dc}=200 V. (b) V_{dc}=300 V. (c) V_{dc}=400 V. (d) V_{dc}=500 V.

TABLE V
THE THEORETICAL VERIFICATION RESULTS

f_i	$GCI_{1,2}(\%)$	$GCI_{2,3}(\%)$	r^pGCI_{12}/GCI_{23}
Maximum magnetic field strength *B*	3.43	6.95	1.03
Hotspot temperature	3.36	12.73	1.08
Maximum electric field *E*	4.60	12.72	1.07

$$p = \frac{\mathrm{In}\left(\dfrac{f_3 - f_2}{f_2 - f_1}\right)}{\mathrm{In}(r)} \tag{28}$$

The characteristic quantity f_i for the magnetic, thermal-airflow, and electric fields are set to maximum *B*, hotspot temperature, and maximum *E* of the HFT. The theoretical verification results are given in Table V. It indicates that the calculation results of $r_pGCI_{1,2}/GCI_{2,3}$ are all close to 1, which means all characteristic quantity results are in the asymptotic range of convergence. The numerical error of magnetic, thermal-airflow, and electric fields simulation based on the fine mesh ($GCI_{1,2}$) is estimated to be 1.31%, 2.98%, and 1.27% respectively, which are within the acceptable level of error of 5 %.

VI. EXPERIMENT VALIDATION

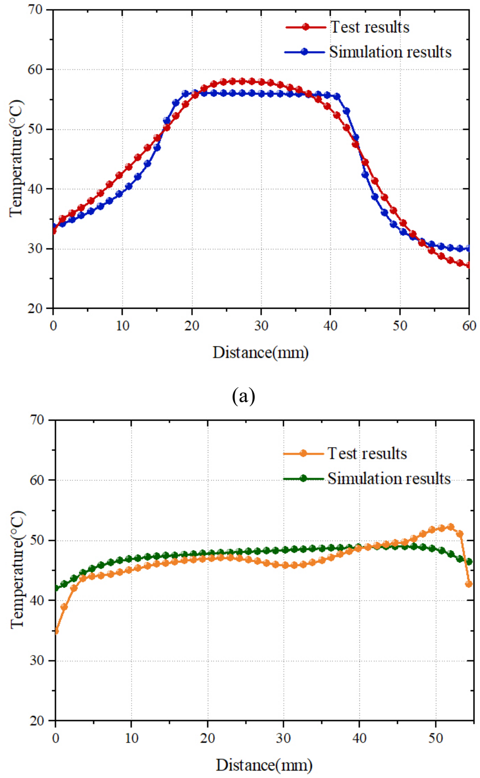

(a)

(b)

Fig. 22. Temperature distribution (a) alone line L_3. (b) alone line L_4 (line L_3 and L_4 are given in Fig. 21d).

A. Test platform setup

To validate the proposed model, a high frequency PWM test platform is developed for the HFT. The circuit diagram and hardware realization of the test platform is shown in Fig. 19. The control signals of the converter are provided by RT Box with Plecs programming. The FLIR E40 thermal camera with a 160×120 60 Hz infrared detector, a thermal sensitivity of 0.07 °C and a temperature range of -20 to 650 °C is used to measure the surface temperature of the transformer. To improve the accuracy of the temperature measurement, the HFT surface is pained black, and the emissivity of the thermal camera is set to 0.98.

B. Electrical and thermal test results

To validate the accuracy of the simulation results, electrical and thermal tests are conducted with V_{dc} is applied to 200, 300, 400, and 500 V, respectively. The measured voltage and current waveforms on both sides of the HFT when V_{dc} is 500 V are given in Fig. 20. When the HFT reached steady state of the thermal equilibrium, its surface temperature measured by the thermal camera are shown in Fig. 21.

Due to the complexity of the multiphysics field inside the transformer, it is challenging or even impossible to measure parameters such as loss density distribution, air flux distribution, internal temperature field distribution, and electric field distribution used to describe the multiphysics field. Therefore, to verify the accuracy of the model, a few parameters and distribution characteristics that are representative and easy to measure are selected. The total EM loss and the transformer surface hot spot temperature values were employed to verify the accuracy of the EM and temperature fields simulation results, respectively. Additionally, two lines along the horizontal and vertical directions of the transformer surface (line L_3 and L_4 are given in Fig. 21d) were used to examine the temperature field variation patterns of the simulated and experimental results, as given in Fig. 22.

TABLE VI
EXPERIMENTAL VALIDATION RESULTS

V_{DC} (V)	Frequency (Hz)	Duty cycle	Loss (W)	Ambient temperature (°C)	Hotspot temperature (°C)	Relative error (%)
200	60000	0.5	2.85	21.9	28.4	4.23
300			7.11	21.9	35.9	0.84
400			11.96	22.3	46.5	0.43
500			24.93	22.5	58.0	0.87

The findings indicate that both exhibit similar variation patterns, and since the temperature field distribution is determined by the loss density distribution, this indicates that the model accurately describes the actual loss density distribution and temperature field distribution pattern of the transformer.

The results show that the hotspot on the surfaces of the HFT occurs slightly above the middle of the insulation, with a hotspot temperature of 28.4, 35.9, 46.5, and 58.0 ℃. The middle part of the insulation adjacent to the winding is subjected to a large thermal stress, and there is a high temperature gradient at the junction of the insulation and the winding. Relative to the insulation layer, the temperature of the core is more uniform. In general, the experimental results present the same distribution characteristics as the simulation results. Table VI shows the comparison between the experiment and simulation results, which shows that the simulation errors are less than 5 %, proving the accuracy of the proposed model.

VII. DISCUSSION

The simulation results reveal that considering electrothermal interactions has a significant impact on the multiphysics field of HFTs. To verify the accuracy and effectiveness of the simulation model, several parameters and characteristics were selected as a basis. A high-frequency PWM test platform for the HFT is established, and electro-thermal tests are conducted at different voltages. The experimental findings demonstrate that the selected parameters have an error margin of 5%, and the simulation model can accurately capture the variation pattern of their distribution. This highlights that the model enhances the accuracy of the simulation and can be utilized to examine the electro-thermal characteristics of insulation withstand as well as identifying its maximum risk point, which can be used for optimal design for HFTs.

The simulation results indicate that the insulation connected to the winding ends is subjected to both a large temperature gradient and electric field strength. The differential expansion or contraction of different parts of insulation material due to a large temperature gradient can cause deformation or warping. To address this issue, epoxy casting can be used to fix the insulation. This method can reduce the mechanical stress on the insulation by filling the gap between the insulation and the winding with epoxy material, providing additional support, and enhancing the insulation level of the insulation system. To improve the electric field strength at this location, the electric field distribution and maximum electric field strength can also be optimized and reduced by applying a non-linear material at triple junctions, changing the arrangement of the windings, and using coils with chamfered edges. Therefore, before implementing these methods, it is necessary to optimize the design and perform simulations using the proposed model, taking into account multiple factors to ensure its effectiveness and reliability.

In this model, the steady-state thermal problem is solved using the time-average loss density as the heat source. This is due to the significant time scale difference between electromagnetic and thermal models. However, the impact of the various stresses resulting from thermal cycling on the insulation could not be accounted for. Therefore, addressing the problem of time scale discrepancy is the direction to improve the proposed model.

The model proposed in this paper contributes to a deeper understanding of the multiphysics within HFTs, particularly in the identification of insulation areas with the greatest risk. Its application extends to optimal design, insulation cooperation, thermal management, and reliability assessment of HFTs. The digital model offers the potential to enhance the distribution of electric fields by simulating different insulation structures and materials, which is crucial in avoiding the risks of PDs caused by the excessive concentration of electric fields. Additionally, the model can be utilized to optimize heat dissipation through simulations of different cooling methods, such as air forced cooling, air natural cooling, fluid cooling, and the use of heat sinks. By considering the comprehensive aspects of electric field distribution, losses, and thermal behavior, the model enables effective optimization of HFT performance and provides valuable insights into their behavior under various operating conditions.

Another important potential application is for the lifetime prediction of HFTs along with life models of insulation. Future research will focus on investigating the aging characteristics of HFTs insulation and developing a life model considering the combined effects of high frequency, high temperature, and high voltage. By integrating these insights with the electrothermal stresses experienced by the insulation, it becomes possible to predict the lifespan of HFTs and provide valuable guidance for their optimal design and practical operation.

VIII. CONCLUSION

In this paper, a comprehensive multi-physics digital model is developed for HFTs that includes circuit, electric, magnetic, loss, and temperature field models. A bidirectional coupling method is proposed, which can considerably enhance the accuracy of the simulation compared to conventional methods. The simulation results of the proposed model and the electrical and thermal stresses on the insulation are demonstrated using a 60k transformer as an example. Finally, experimental validation is performed to verify the accuracy of the proposed model and the results demonstrate that it can achieve similar electrical and thermal characteristics with the HFT. The model can be utilized for optimal design and reliability assessment of HFTs.

REFERENCES

[1] Q. Zhu, L. Wang, A. Q. Huang, K. Booth and L. Zhang, "7.2-kV Single-Stage Solid-State Transformer Based on the Current-Fed Series Resonant Converter and 15-kV SiC mosfets," IEEE Transactions on Power Electronics, vol. 34, no. 2, pp. 1099-1112, Feb. 2019, doi: 10.1109/TPEL.2018.2829174.

[2] P. L. Métayer, Q. Loeuillet, F. Wallart, C. Buttay, D. Dujic and P. Dworakowski, "Phase-Shifted Full Bridge DC–DC Converter for Photovoltaic MVDC Power Collection Networks," IEEE Access, vol. 11, pp. 19039-19048, 2023, doi: 10.1109/ACCESS.2023.3247952.

[3] K. Basu, A. Shahani, A. K. Sahoo and N. Mohan, "A Single-Stage Solid-State Transformer for PWM AC Drive With Source-Based Commutation of Leakage Energy," IEEE Transactions on Power Electronics, vol. 30, no. 3, pp. 1734-1746, March 2015, doi: 10.1109/TPEL.2014.2320996.

[4] Wang W, Wang X, He J, Liu Y, Li S, Nie Y. "Electric stress and dielectric breakdown characteristics under high-frequency voltages with multi-harmonics in a solid-state transformer, " International Journal of Electrical Power & Energy Systems. July 2021.

[5] Ren, H., Tanaka, Y., Miyake, H., Li, Q., Gao, H., Li, C. and Wang, Z., 2021. "Effect of sinusoidal waveform and frequency on space charge characteristics of polyimide," High Voltage, 6(5), pp.760-769.

[6] G. C. Montanari, G. Mazzanti and L. Simoni, "Progress in electrothermal life modeling of electrical insulation during the last decades," IEEE Transactions on Dielectrics and Electrical Insulation, vol. 9, no. 5, pp. 730-745, Oct. 2002, doi: 10.1109/TDEI.2002.1038660.

[7] Q. Wang, H. Wang, Z. Peng, P. Liu, T. Zhang and W. Hu, "3-D coupled electromagnetic-fluid-thermal analysis of epoxy impregnated paper converter transformer bushings," IEEE Transactions on Dielectrics and Electrical Insulation, vol. 24, no. 1, pp. 630-638, Feb. 2017, doi: 10.1109/TDEI.2016.005641.

[8] E. E. Lesniewska and J. Olak, "Improvement of the Insulation System of Unconventional Combined Instrument Transformer Using 3-D Electric-Field Analysis," IEEE Transactions on Power Delivery, vol. 33, no. 6, pp. 2582-2589, Dec. 2018, doi: 10.1109/TPWRD.2017.2725381.

[9] A. Santisteban, F. Delgado, A. Ortiz, I. Fernández, C. J. Renedo and F. Ortiz, "Numerical analysis of the hot-spot temperature of a power transformer with alternative dielectric liquids," IEEE Transactions on Dielectrics and Electrical Insulation, vol. 24, no. 5, pp. 3226-3235, Oct. 2017, doi: 10.1109/TDEI.2017.006228.

[10] T. O. Olowu, H. Jafari, M. Moghaddami and A. I. Sarwat, "Multiphysics and Multiobjective Design Optimization of High-Frequency Transformers for Solid-State Transformer Applications," IEEE Transactions on Industry Applications, vol. 57, no. 1, pp. 1014-1023, Jan.-Feb. 2021, doi: 10.1109/TIA.2020.3035129.

[11] B. Chen, X. Liang and N. Wan, "Design Methodology for Inductor-Integrated Litz-Wired High-Power Medium-Frequency Transformer With the Nanocrystalline Core Material for Isolated DC-Link Stage of Solid-State Transformer," IEEE Transactions on Power Electronics, vol. 35, no. 11, pp. 11557-11573, Nov. 2020, doi: 10.1109/TPEL.2020.2987944.

[12] M. Mogorovic and D. Dujic, "FEM-Based Statistical Data-Driven Modeling Approach for MFT Design Optimization," IEEE Transactions on Power Electronics, vol. 35, no. 10, pp. 10863-10872, Oct. 2020, doi: 10.1109/TPEL.2020.2982130.

[13] S. Zhao, Q. Li, F. C. Lee and B. Li, "High-Frequency Transformer Design for Modular Power Conversion From Medium-Voltage AC to 400 VDC," IEEE Transactions on Power Electronics, vol. 33, no. 9, pp. 7545-7557, Sept. 2018, doi: 10.1109/TPEL.2017.2774440.

[14] Guo, Zhicheng, Sanjay Rajendran, Jagadeesh Tangudu, Yasmin Khakpour, Stephen Taylor, Lei Xing, Yue Xu, Xianyong Feng, and Alex Q. Huang. "A Novel High Insulation 100 kW Medium Frequency Transformer." IEEE Transactions on Power Electronics, vol. 38, no. 1, pp. 112-117, Jan. 2023, doi: 10.1109/TPEL.2022.3205646.

[15] Shafaei, Rouhollah, Maria Celeste Garcia Perez, and Martin Ordonez. "Planar transformers in LLC resonant converters: High-frequency fringing losses modeling." IEEE Transactions on Power Electronics, vol. 35, no. 9, pp. 9632-9649, Sept. 2020, doi: 10.1109/TPEL.2020.2971424.

[16] Yi, Z., Sun, K., Liu, H., Cao, G. and Lu, S., 2021. Design and optimization of the insulation of medium-voltage medium-frequency transformers for solid-state transformers. IEEE Journal of Emerging and Selected Topics in Power Electronics, vol. 10, no. 4, pp. 3561-3570, Aug. 2022, doi: 10.1109/JESTPE.2021.3094674.

[17] M. Leibl, G. Ortiz and J. W. Kolar, "Design and Experimental Analysis of a Medium-Frequency Transformer for Solid-State Transformer Applications," IEEE Journal of Emerging and Selected Topics in Power Electronics, vol. 5, no. 1, pp. 110-123, March 2017, doi: 10.1109/JESTPE.2016.2623679.

[18] Maxwell help, ANSYS, Inc., Canonsburg, PA, USA, 2021

[19] Faro, A. A. "Navier-Stokes Equation (An overview and the simplification)." The discourse, 2020.

[20] Narasimhan, Thiruppudaimarudhur N., "Fourier's heat conduction equation: History, influence, and connections." Reviews of Geophysics 37.1, pp. 151-172, 1999.

[21] Icepak help, ANSYS, Inc., Canonsburg, PA, USA, 2021

[22] Matula, R.A, "Electrical resistivity of copper, gold, palladium, and silver." Journal of Physical and Chemical Reference Data 8.4, pp. 1147-1298, 1979.

[23] Steinmetz, Chas Proteus, "On the law of hysteresis." Transactions of the American Institute of Electrical Engineers 9.1 pp. 1-64, 1892.

[24] I. Villar, U. Viscarret, I. Etxeberria-Otadui and A. Rufer, "Global Loss Evaluation Methods for Nonsinusoidally Fed Medium-Frequency Power Transformers," IEEE Transactions on Industrial Electronics, vol. 56, no. 10, pp. 4132-4140, Oct. 2009, doi: 10.1109/TIE.2009.2021174.

[25] M. Kaymak, Z. Shen and R. W. De Doncker, "Comparison of analytical methods for calculating the AC resistance and leakage inductance of medium-frequency transformers," 2016 IEEE 17th Workshop on Control and Modeling for Power Electronics (COMPEL), Trondheim, Norway, 2016, pp. 1-8, doi: 10.1109/COMPEL.2016.7556740.

[26] Guo, Zhicheng, Alex Q. Huang, Robert E. Hebner, Gian Carlo Montanari, and Xianyong Feng. "Characterization of Partial Discharges in High-Frequency Transformer Under PWM Pulses." IEEE Transactions on Power Electronics, vol. 37, no. 9, pp. 11199-11208, Sept. 2022, doi: 10.1109/TPEL.2022.3169747.

[27] Duy, C.T., Bonifaci, N., Denat, A., Lesaint, O., Caliap, L., Girodet, A., Gelloz, B. and Ponchon, P., "Partial discharges at a triple junction metal/solid insulator/gas and simulation of inception voltage," Journal of Electrostatics, 66(5-6), pp.319-327, 2008.

[28] T. S. Sudarshan and R. A. Dougal, "Mechanisms of Surface Flashover Along Solid Dielectrics in Compressed Gases: a Review," IEEE Transactions on Electrical Insulation, vol. EI-21, no. 5, pp. 727-746, Oct. 1986, doi: 10.1109/TEI.1986.348922.

[29] Trinh, N.G., "Failure Mechanisms of Gas Insulation and at Gas-Insulator Interface: Their Influence on Gas-Insulated Equipment," Gaseous Dielectrics VI, pp.517-529, 1991.

[30] Deželak, Klemen, Martin Petrun, Miran Rošer, Drago Dolinar, and Gorazd Štumberger. "The impact of iron core model on dynamic behavior of three-phase power transformer dynamic model." IEEE Transactions on Magnetics, vol. 51, no. 1, pp. 1-4, Jan. 2015, Art no. 8400104, doi: 10.1109/TMAG.2014.2357075.

[31] Marketos, Philip, and Turgut Meydan. "Novel transformer core design using consolidated stacks of electrical steel." IEEE Transactions on Magnetics, vol. 42, no. 10, pp. 2821-2823, Oct. 2006, doi: 10.1109/TMAG.2006.879139.

[32] Liu, C., Qi, L., Cui, X., Shen, Z. and Wei, X., 2015. Wideband mechanism model and parameter extracting for high-power high-voltage high-frequency transformers. IEEE Transactions on Power Electronics, vol. 31, no. 5, pp. 3444-3455, May 2016, doi: 10.1109/TPEL.2015.2464722.

[33] Roache, Patrick J., "Perspective: a method for uniform reporting of grid refinement studies." pp. 405-413, 1994.

Zhaoxin Wang (Student Member, IEEE) was born in Henan, China, in 1994. She received the M.S. degree in electrical engineering from North China Electric Power University, Hebei, China, in 2020. She is currently working toward the Ph.D. degree in electrical engineering with Aalborg University, Aalborg, Denmark.

Her research interests include multiphysics modeling of high frequency transformers, and the aging and endurance of insulation for power electronics applications.

Claus Leth Bak was born in Århus, Denmark, on April 13th, 1965. He received the B.Sc. with honors in Electrical Power Engineering in 1992 and the M.Sc. in Electrical Power Engineering at the Department of Energy Technology at Aalborg University in 1994. After his studies he worked as a professional engineer with Electric Power Transmission and Substations with specializations within the area of Power System Protection at the NV Net Transmission System Operator. In 1999 he was employed as an Assistant Professor at the Department of Energy Technology, Aalborg University. He received Full Professor position in 2011. He received the PhD degree in 2015 with the thesis "EHV/HV underground cables in the transmission system". He has supervised/co-supervised +45 PhD's and +50 MSc theses. His main Research areas include Corona Phenomena on Overhead Lines, Composite Transmission Towers, Power System Modeling and Transient Simulations, Underground Cable transmission, Power System Harmonics, Power System Protection, composite materials for EHV power pylons and HVDC-VSC Offshore Transmission Networks. He is the author/coauthor of app. 440 publications. He is chair of the Danish Cigré National Committee, former member of CIGRE Technical Council and member of Cigré SC C4 AG1 and D1. He is an IEEE senior member (M'1999, SM'2007). He received the DPSP 2014 best paper award and the PEDG 2016 best paper award. He received CIGRE Distinguished member award (2020) and CIGRE TC award (2020). He serves as Head of the Energy Technology PhD program (+ 130 PhD's) and as Head of the Section of Electric Power Systems and Microgrids and is a member of the PhD board at the Faculty of Engineering and Science.

Huai Wang (Senior Member, IEEE) received the B.E. degree in electrical engineering from the Huazhong University of Science and Technology, Wuhan, China, in 2007, and the Ph.D. degree in power electronics from the City University of Hong Kong, Hong Kong, in 2012.

He is currently a Professor with AAU Energy, Aalborg University, Aalborg, Denmark, where he leads the Group of Reliability of Power Electronic Converters (ReliaPEC) and the mission on Digital Transformation and AI. He was a Visiting Scientist with ETH Zurich, Switzerland, from August to September 2014, and with the Massachusetts Institute of Technology, Cambridge, MA, USA, from September to November 2013. He was with the ABB Corporate Research Center, Switzerland in 2009. His research interests include the fundamental challenges in modeling and validation of power electronic component failure mechanisms and application issues in system-level predictability, condition monitoring, circuit architecture, and robustness design. Dr. Wang was the recipient of the Richard M. Bass Outstanding Young Power Electronics Engineer Award from the IEEE Power Electronics Society, in 2016, and the 1st Prize Paper Award from IEEE TRANSACTIONS ON POWER ELECTRONICS, in 2021. He serves as an Associate Editor for the Journal of Emerging and Selected Topics in Power Electronics and IEEE TRANSACTIONS ON POWER ELECTRONICS.

Henrik Sørensen received the M.Sc. degree from Aalborg University, Aalborg, Denmark, in 1999, the Ph.D. degree in 2006, and the master's degree in public governance from Aalborg University in 2021. He is currently an Associate Professor and the Head of the Section for Thermal Engineering, Department of Energy, Aalborg University. In 2015, he completed the Leadership Development Program at the European Consortium of Innovative Universities. He has been appointed as the Head of Section since 2008. His research interests are fluid mechanics, multiphase flow, and heat transfer.

Filipe Faria da Silva (Senior Member, IEEE) received the M.Sc. degree in electrical and computers engineering from the Instituto Superior Técnico, Lisbon, Portugal, in 2008 and the Ph.D. degree in electric power systems from Aalborg University, Aalborg, Denmark, in 2011. In 2008, he was with EDP-Labelec and from 2008 to 2011, with Danish TSO Energinet. He is currently an Associate Professor with the Department of Energy Technology, Aalborg University, where he is also Semester Coordinator for the Electrical Power System and High Voltage Engineering Master Program and the Leader of the Modern Power Transmission Systems Research Program. His research interests include power cables, electromagnetic transients and insulation coordination, power quality, network stability, HVDC transmission, and HV phenomena.